Experiments in Fluids (2024) 65:146
https://doi.org/10.1007/s00348-024-03885-y

RESEARCH ARTICLE

Three-dimensional flow features of underexpanded jets emerging from an elliptic convergent nozzle

Tatsuya Nagata[1] · Takumi Sakashita[1] · Shinichiro Nakao[1] · Yoshiaki Miyazato[1]

Received: 12 July 2024 / Revised: 7 September 2024 / Accepted: 9 September 2024
© The Author(s), under exclusive licence to Springer-Verlag GmbH Germany, part of Springer Nature 2024

Abstract

Understanding the fundamental structure of shock-containing elliptic jets is of great academic and engineering interest, but there are still many unknowns. The three-dimensional flow features of an underexpanded jet emerging from an elliptic convergent nozzle with an aspect ratio of 4.0 at the exit face are experimentally investigated by rainbow schlieren tomography (RST). The elliptic jet is discharged into quiescent air using an intermittent blowdown wind tunnel. The Reynolds number based on the equivalent diameter and flow properties at the nozzle exit is 3.0×10^5. Multi-view rainbow schlieren images of the elliptic jet are taken by rotating the nozzle around its longitudinal axis, and the density field is reconstructed using the convolution back-projection (CBP) method. The three-dimensional density field of the elliptic jet is acquired with a nominal spatial resolution of approximately 13 µm. The flow characteristics of shock-containing elliptic jets, such as the shock-cell length, the supersonic length, the switchover location, and the axis-switching location, are quantitatively revealed from the streamwise density profiles, the density contour plots in the minor-axis and major-axis planes where a method is proposed to quantitatively estimate the switchover and axis-switching locations. The shock-cell and supersonic lengths are quantitatively compared with the recently introduced analytical solution and scaling law, respectively. In addition, the shock structures and topology showing the spatial evolution in the streamwise direction of the near-field shock system within the elliptic jet are experimentally demonstrated for the first time.

1 Introduction

Supersonic jets are actively used across a considerable number of fields, including aerospace engineering, mechanical engineering, and the agricultural industry. In the field of aeronautical engineering, much effort has been devoted to the research and development of hypersonic aircrafts in recent decades because of its revolutionary applications in commercial aviation as a fast, long-range method of transporting passengers around the globe (Urzay 2018). One of the barriers to the development of hypersonic aircrafts is supersonic combustion, where the fuel and oxidizer are burnt under supersonic velocity conditions in the combustor (Urzay 2018). The fuel injected into the combustor through an injector nozzle must be mixed at the molecular level with the oxygen present in the intake air stream. The shape of the injector nozzle would be a key factor in one of the solutions to enhance the mixing and combustion process in the airbreathing hypersonic propulsion system. The previous studies have focused on supersonic jets from either axisymmetric nozzles (Franquet et al. 2015) or rectangular nozzles (Edgington-Mitchell 2019). On the other hand, it has been widely recognized that nozzles with an elliptic shape at the exit face have numerous advantages when compared with conventional round and rectangular nozzles such as improvements in flow mixing within the supersonic jets (Kinzie and McLaughlin 1999), shorter potential core length (Aravindh Kumar and Rathakrishnan 2016, 2017), enhanced shear layer entrainment, and reduced shock-associated noise under

Takumi Sakashita, Shinichiro Nakao, and Yoshiaki Miyazato have contributed equally to this work.

✉ Yoshiaki Miyazato
miyazato@kitakyu-u.ac.jp

Tatsuya Nagata
ntatsuya120122@gmail.com

Takumi Sakashita
sakataku66@gmail.com

Shinichiro Nakao
s-nakao@kitakyu-u.ac.jp

[1] Department of Mechanical Systems Engineering, The University of Kitakyushu, 1-1 Hibikino, Wakamatsu-ku, Kitakyushu 808-0135, Japan

Published online: 24 September 2024

particular operating conditions (Gutmark and Grinstein 1999), and the separation control in supersonic crossflow (Sebastian and Schreyer 2022).

Kinzie and McLaughlin (1999) experimentally investigated the aerodynamic and acoustic properties of shock-free supersonic jets issuing from circular and elliptic nozzles with a design Mach number of 1.5 and demonstrated beneficial properties of the elliptic jet in terms of increased mixing and noise reduction compared to the round jet. The acoustic properties or turbulent structures of shock-containing elliptical jets were studied intensively by Mitchell et al. (2013); Edgington-Mitchell et al. (2015a, 2015b); Kalyan and Karabasov (2017); Li et al. (2017); and Rao et al. (2020). Edgington-Mitchell et al. (2015b) demonstrated staging behavior in screeching elliptic jets including the varicose, flapping, and helical modes using particle image velocimetry (PIV) and a high-speed schlieren technique. Kalyan and Karabasov (2017) proposed a mixed-scale model to predict broadband shock-associated noise in axisymmetric and asymmetric shock-containing jets using an improved turbulence scale model, and showed that for the same thrust conditions, the elliptic nozzles lead to noise reduction at the source compared to the baseline axisymmetric jets. Rao et al. (2020) investigated the screech characteristics of underexpanded sonic jets flowing from an elliptic convergent nozzle. The screeching behavior and the closure mechanism of a feedback loop for the flapping mode of shock-containing elliptic jets were clarified from time-resolved schlieren images and near-field acoustic data using the proper orthogonal decomposition (POD) and dynamic mode decomposition (DMD) methods.

A peculiar phenomenon associated with subsonic and supersonic elliptical jets is axis-switching (Hussain and Husain 1989; Zaman 1996), in which the jet cross-section expands in the direction of the minor axis and contracts in the direction of the major axis, resulting in a 90° switch after a certain downstream distance. In the case of subsonic elliptic jets, Hussain and Husain (1989) provided significant insight into the mechanism of axis-switching from velocity measurements inside the jets using a hot-wire anemometer. They referred to the location at which axis-switching begins as a “switchover location.” Note that a supersonic elliptic jet becomes almost circular at the point where the minor and major axes of the jet are almost identical (Aravindh Kumar and Rathakrishnan 2017). There are limited experimental studies of axis-switching observed in supersonic elliptical jets (Mitchell et al. 2013; Edgington-Mitchell et al. 2015a; Chauhan et al. 2015; Aravindh Kumar and Rathakrishnan 2016, 2017). It is very important to know the characteristics of axis-switching because it is closely related to mixing enhancement (Aravindh Kumar and Rathakrishnan 2017).

Edgington-Mitchell et al. (2015a) experimentally investigated the multimodal instability of an underexpanded elliptic jet with an aspect ratio (AR) of 2 at a nozzle pressure ratio (NPR) of 2.2 using PIV and schlieren imaging where the AR is defined as the ratio of the major axis to the minor axis at the cross-section of the nozzle exit, and the NPR is defined as the ratio of the stagnation pressure upstream of the nozzle to the back pressure. They showed that the presence of shock-cells results in much faster axis-switching, and it is responsible for the production of helical instability. Chauhan et al. (2015) experimentally studied the mixing characteristics of underexpanded sonic jets originating from an elliptic convergent nozzle of AR = 2.0 at NPRs of two to five in steps of one using Pitot tube surveys and the shadowgraph technique. The results of the experiments show that the axis-switching location shifts upstream with an increase in NPR, implying that the near-field mixing is enhanced with increasing NPR. The earlier axis-switching is an indication of faster spread and faster near-field mixing of the jet with the entrained fluid from the surrounding (Aravindh Kumar and Rathakrishnan 2017).

Analytical studies of slightly underexpanded elliptic jets were performed by Nagata et al. (2022) and Islam et al. (2024). Nagata et al. (2022) proposed an analytical model on shock-cell spacings of underexpanded jets emerging from elliptic convergent nozzles with various ARs and NPRs. The proposed model was found to be in good quantitative agreement with the experimental data for ARs = 1, 2, and 8. Islam et al. (2024) derived analytical solutions of weakly expanded elliptic jets using the vortex sheet model. Perumal and Rathakrishnan (2021) conducted a systematic study of shock-containing elliptic jets emerging from elliptic nozzles with various ARs and design Mach numbers to derive semi-empirical relations of the supersonic core length. On the other hand, numerical studies of supersonic elliptic jets have been performed by Menon and Skews (2010), Li et al. (2017), and Mirjalily (2021). However, there was no quantitative experimental data on supersonic elliptical jets to validate the numerical codes. Therefore, Menon and Skews (2010), and Li et al. (2017) validated their numerical results using experimental data for "axisymmetric" underexpanded jets before performing numerical simulations for supersonic elliptical jets. Mirjalily (2021) used previous experimental values of the Pitot pressures along the central axis of a supersonic elliptic jet to validate numerical codes.

Even recently, much remains unknown about the internal structure of the shock-containing elliptic jets due to the limitations of measurement techniques. For instance, for the shock shape in the major-axis plane of an underexpanded jet issuing from an elliptic convergent nozzle of AR = 2 at NPR = 5.6, a shadowgraph image by Menon and Skews (2010) captures a Mach stem, while the simulation by Li et al. (2017) produces an X-shaped shock instead of a Mach shock. In addition, the numerical simulations performed by Li et al. (2017) show that the shock-cell lengths, when

normalized to the equivalent diameter, are nearly the same for underexpanded jets issuing from round (AR = 1) and elliptic (AR = 2) convergent nozzles. However, recent analytical and experimental results of Nagata et al. (2022) demonstrate that the shock-cell length in elliptic underexpanded jets decreases with increasing AR, even if the equivalent diameter remains the same.

Inserting an intrusive probe into supersonic flow has serious effects on the flow field, such as the generation of shocks. Laser Doppler anemometry (LDA) and particle image velocimetry (PIV) with seed particles have the inevitable problem that the tracer particles do not follow the flow immediately after the shock (Feng and McGuirk 2016; Yüceil 2017). In contrast, laser interferometry such as Mach–Zehnder interferometry with the finite-fringe setting (Sugawara et al. 2020; Sugawara et al. 2021) and multi-view digital holographic interferometry (Léon et al. 2022) can capture three-dimensional density fields of shock-containing jets without tracer particles. However, laser-based equipment is generally expensive and requires skilled optical adjustment.

On the other hand, the recent advent of high-performance computers and the development of large storage devices, as well as the processing of large amounts of data through machine learning, have enabled quantitative flow visualization techniques that were previously extremely difficult to realize because the three-dimensional structure of asymmetric jets must be numerically captured by applying processing based on the principles of computed tomography to two-dimensional images projected from multiple viewing directions. Background-oriented schlieren (BOS) is undoubtedly the most significant recent development in the field of quantitative flow visualization (Settles and Hargather 2017). Recently, BOS has made it possible to perform multi-view images of the flow using multiple cameras simultaneously and then obtain an instantaneous three-dimensional structure of the density or temperature field based on the principles of computed tomography (Nicolas et al. 2017; Grauer et al. 2018; Kirby 2018; Amjad et al. 2020; Akamine et al. 2023). Meanwhile, rainbow schlieren tomography (RST) (Takano et al. 2016; Maeda et al. 2018; Fukunaga et al. 2022), a type of quantitative flow visualization comparable to BOS, can acquire the density field with high precision and high spatial resolution (Agrawal and Wanstall 2018).

The primary objective of the present study is to understand the fundamental structure of a shock-containing elliptic jet from academic and engineering perspective. To achieve this goal, the three-dimensional density field of the elliptic jet is acquired by RST with the convolution back-projection (CBP) method. To the best of the author's knowledge, currently, the suitable experimental data of shock-containing elliptic jets needed to validate the computational code do not exist. The authors, therefore, consider that it is also important to obtain benchmark experimental data for the validation of numerical calculations. In addition, the flow features of shock-containing elliptic jets including the shock-cell length, supersonic length, switchover location, and axis-switching location, are extracted by analyzing the density field. The validity of the analytical model (Nagata et al. 2022) for the shock-cell length and the scaling law (Perumal and Rathakrishnan 2021) for the supersonic length is then clarified using the present experimental values. It should be noted that the switchover and axis-switching locations have not been quantitatively defined in most studies and remain ambiguous. Therefore, in the present study, we propose a method to quantitatively estimate these locations from jet density fields. Furthermore, the shock structures and topology in the first shock-cell of the elliptic jet are experimentally demonstrated for the first time.

2 Experimental methods

2.1 Measurement systems and test nozzle

The experiments are conducted in a blowdown compressed air facility. Ambient air is pressurized by the compressor up to 1 MPa and stored in a high-pressure reservoir comprising two storage tanks with a total capacity of 2 m^3 after filtering and drying. The high-pressure dry air from the reservoir stagnates in the plenum chamber, as shown in Fig. 1; subsequently, it is discharged into the atmosphere through a test nozzle that can be rotated around its longitudinal axis. The desired NPR($= p_{os}/p_b$) is achieved by changing the plenum pressure, p_{os}, with the back pressure, p_b (= atmospheric pressure: 101.8 kPa), held constant at 4.0 to produce

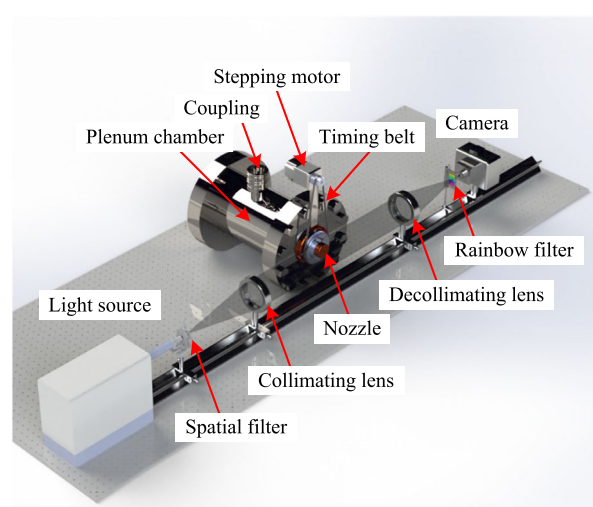

Fig. 1 Schematic drawing of the blowdown compressed air facility with a rainbow schlieren optical system

underexpanded jets including strong shocks such as a Mach stem.. The ambient temperature, T_b, is 298.5 K.

As shown in Fig. 2a in the form of a cut model, an elliptic convergent nozzle of AR = 4 with a lip wall of 52 mm outer diameter is used as a test nozzle. As shown in Fig. 2b, the nozzle wall contour from the inlet to exit is designed based on a sinusoidal curve to provide smooth uniform flows at the inlet and exit. Note that Donaldson and Gray (1966) showed that the outer configuration of a nozzle affects the decay and spreading rates of subsonic and supersonic jets, but this is not mentioned in this study. The effect of the nozzle lip on the flow features of a supersonic elliptical jet is left for future research. The axial length from the nozzle inlet to the exit is 75 mm; the nozzle has an elliptic cross-section with an aspect ratio of 4 at each axial position. The semi-major and semi-minor axes of the nozzle inlet are 30 ± 0.05 mm and 7.5 ± 0.05 mm, respectively, and the corresponding ones at the nozzle exit are $L_a = 5.0 \pm 0.05$ mm and $L_b = 1.25 \pm 0.05$ mm, respectively. The Cartesian coordinate system (x, y, z) is employed with its origin at the center of the nozzle exit plane; the x-, y-, and z-axes are oriented along the directions of the major axis, minor axis, and jet central axis, respectively.

The nozzle is manufactured using a 3D printer (Flashforge, Adventurer 3X) based on fused deposition modeling, where the melt extrusion method was used to deposit filaments of thermoplastic based on a specific pattern. The wall shape at the nozzle exit section and the wall roughness inside the nozzle play an important role for the flow features of jets emerging from the test nozzle. Hence, we obtained a digital image of the nozzle exit section by the laser scanning microscope (Olympus, LEXT OLS4100) and then measured the wall shape against the polar angle θ as shown in Fig. 3. The red line is the design curve of the ellipse, and the open symbols show the measured values. Excellent quantitative agreement is reached between the design curve and measurement data with a standard deviation of about 37 µm. In addition, the arithmetic wall roughness, R_a, inside the nozzle was measured by the surface roughness measuring machine (Mitutoyo, SV-C524) with a resolution of 0.05 µm for vertical and horizontal directions, resulting in 6.37 µm. There would be an effect of wall roughness on the flow characteristics of elliptic jets. This is left as an issue for future research.

The equivalent diameter D_{eq} at the nozzle exit face is defined as the diameter of a virtual circle with the same cross-sectional area as the actual nozzle area (Hussain and Husain 1989). It is given by $D_{eq} = 2(L_a L_b)^{1/2} = 5$ mm for the present nozzle. This lengthscale can adequately characterize jet behavior and has been used successfully in the past

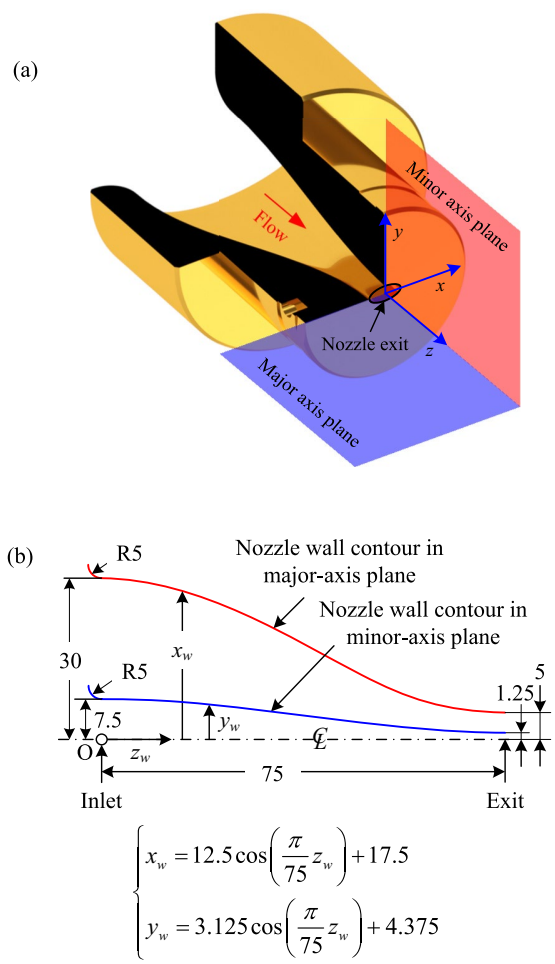

Fig. 2 Schematic diagram of a test nozzle with the **a** cut model of the elliptic convergent nozzle with the Cartesian coordinate system (x, y, z) as well as **b** the nozzle wall contours in the minor-axis and major-axis planes. All dimensions are in mm

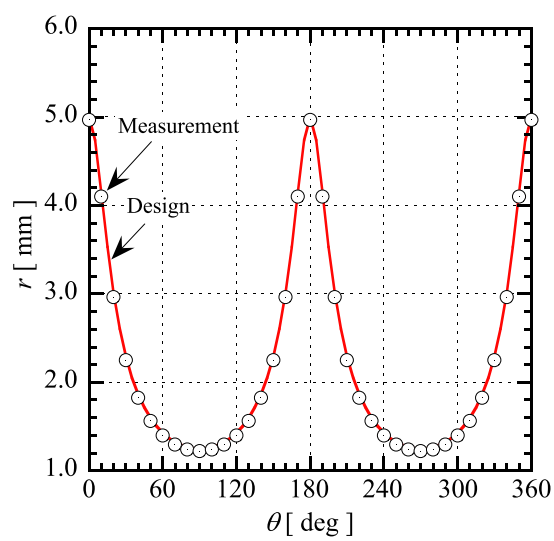

Fig. 3 Wall shape at the nozzle exit section against the polar angle. The red line denotes the design curve for an ellipse with semi-major and semi-minor axes of 5 mm and 1.25 mm, respectively, and the open symbols are measured values

to compare data for supersonic jets emerging from nozzles with the same exit area but different geometries such as circular, rectangular, diamond, and elliptic (Alvi et al. 1996). Li et al. (2017) numerically investigated flow characteristics of highly underexpanded jets at the same NPR of 5.6 but issuing from four different convergent nozzles with the circular, elliptic, square, and rectangular shapes at the exit. The streamwise positions of the first three shocks along the jet centerline, normalized by D_{eq}, were found to be in good agreement for different jets (Li et al. 2017). Note that the hydraulic diameter D_h is defined as four times the cross-sectional area divided by the wetted perimeter (Streeter et al. 2007). For the present nozzle, $D_h = 3.66$ mm. The hydraulic diameter is very useful in duct flows where friction losses dominate.

2.2 Rainbow schlieren deflectometry

As shown in Fig. 1, jet flow fields are visualized through rail-mounted optical components, including a spatial filter with a rectangular source aperture of 3 mm × 50 µm; two achromatic lenses with a diameter and focal length of 100 mm and 500 mm, respectively; a rainbow filter with a continuous hue variation at a width of 2.4 mm; and a digital camera fitted with a focusing lens (Nikon Bellows PB-6, an extension range of 48–208 mm). A continuous 250 W metal halide light source (Sigmakoki, IMH-250) connected to a fiber-optic cable with a diameter of 50 µm provides light input to the spatial filter through an objective lens with a focal length of 16.56 mm. The rainbow filter is introduced into the back focal plane (schlieren cutoff plane) of the decollimating lens. When focusing on the shock structures in jet flow fields, the filter is placed in such a manner that the hue changes in the z-direction. On the other hand, when focusing on changes in jet boundaries and shear layers, the filters are arranged so that the hue changes in the directions perpendicular to the z-direction (x- or y-direction). These filter settings correspond to the vertical knife edge and horizontal knife edge in the conventional schlieren optical system. We refer to the former as the vertical filter setting and the latter as the horizontal filter setting.

A digital camera (Nikon D7100, 6000 × 4000 square pixel resolution with a 14-bit pixel depth) is used to capture the density field of a shock-containing elliptic jet. Multi-view rainbow schlieren images of the jet are taken by rotating the nozzle around its longitudinal axis at equal intervals of $\Delta\theta = 5$ deg (angular resolution) from 0 to 180 deg with the horizontal filter setting. To reduce measurement errors, each rainbow schlieren image taken at a rotation angle between 0 and 90 deg is averaged with the corresponding image taken in the range of 90–180 deg to account for nozzle symmetry. As a reference for angular resolution, Agrawal et al. (1998) measured temperature distributions in an incompressible jet issuing from an inclined round nozzle using a thermocouple probe and RSD. Temperature fields from RSD were reconstructed using multi-view rainbow schlieren images taken at 7.2 degree angular resolution, and the average relative difference between the thermocouple and schlieren measurements was found to be 1.2%. Fukunaga et al. (2022) have recently successfully captured the three-dimensional density field of a rectangular underexpanded jet using RSD with 5 degree angular resolution. Nicolas et al. (2017) conducted a three-dimensional BOS experiment using 12 cameras mounted at 15-degree intervals around an underexpanded jet. Léon et al. (2022) used multi-view digital holographic interferometry with 30 degree angular resolution to measure the instantaneous density field of a screeching underexpanded jet in helical mode.

Rainbow schlieren pictures of the elliptic jets are taken with an exposure time of 1/8000 s and ISO400 with a continuous schlieren light source at NPR = 4.0. The center of the jet is in focus. Five schlieren images are recorded for each rotation angle of the nozzle to estimate statistical information such as the average and standard deviation. The camera outputs of the rainbow schlieren images in RGB format are transferred onto a personal computer hard drive using Nikon Camera Control Pro software and then stored as JPEG files. Each JPEG RGB image (8-bit each) is turned into an HSI image (8-bit each) according to the hue (H)-saturation (S)-intensity (I) representation obtained from direct transformation of the RGB tristimulus values. Only the transformed hue (H) values are utilized to calculate the ray shift at the cutoff plane of the schlieren system.

An in-house rainbow filter with 2.4 mm in width by 35 mm in length is utilized in the present study. An image of the rainbow filter is shown with the calibration curve in Fig. 4a. In the HSI color representation, the hue (color) of the rainbow filter changes continuously from the left to right ends, and a physical quantity from 0 to 360 deg is assigned to the hue at each position. In the present experiment, since a single parameter H with an 8-bit image (256 gradation levels) is assigned to the width (2.4 mm) of the rainbow filter. It means that the filter resolution is approximately 9.4 µm, and it is about one-fifth the source image size (50 µm) of the rainbow filter.

The rainbow filter is calibrated by moving it parallel and perpendicular about the vertical and horizontal filter settings, respectively, with respect to the nozzle central axis in intervals of 10 μm just before starting the experiments. The calibration curves for the vertical and horizontal filter settings are shown in Fig. 4b, c, respectively. The open symbols express the experimental data with a maximum precision error of approximately 3 deg on the hue values. The solid line indicates a least squares regression line of the calibration data, which is given by a fifth-order polynomial. The background hue in the rainbow filter for

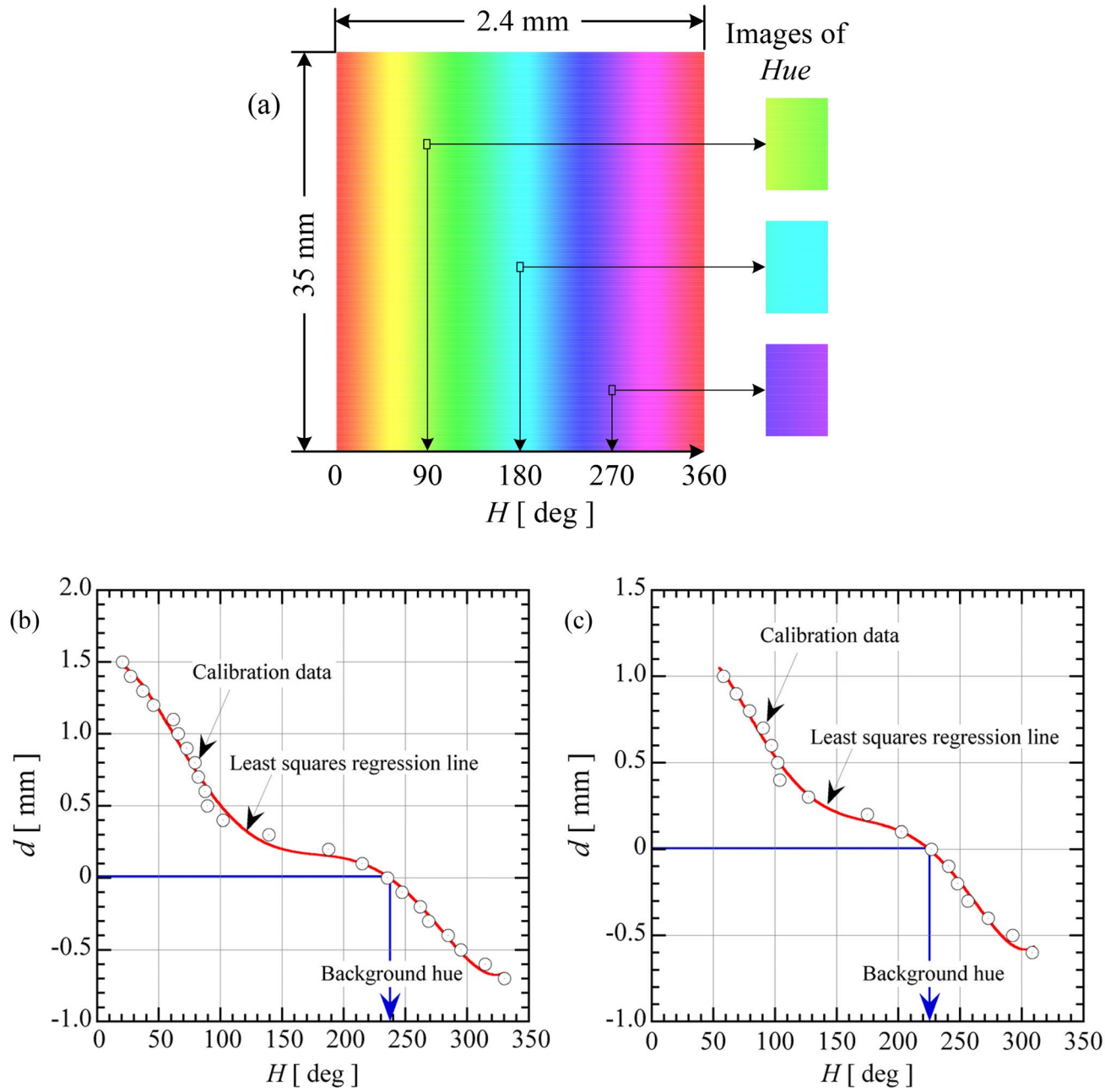

Fig. 4 The calibration characteristics of a rainbow filter. **a** An image of the rainbow filter with representative hues at $H = 90$, 180, and 270 degrees. Calibration curves for **b** the vertical and **c** horizontal cutoff settings of the rainbow filter

the present experiment corresponds to the location shown as the blue arrow. The calibration curve for the vertical filter setting can be utilized when the spatial evolution of the streamwise density gradient is qualitatively known (Nagata et al. 2022). The details of how to properly design, generate, and calibrate a rainbow filter are described in Agrawal and Wanstall (2018). Jet density fields can only be reconstructed from rainbow schlieren images taken with the horizontal filter setting using the CBP method as described in Sect. 2.3.

2.3 Reconstruction of jet density fields

A light ray traveling in a cross-section (x, y plane) of an asymmetric jet emerging from a nozzle is shown in Fig. 5 where the Cartesian coordinate system (x,y,z) is used. The z-axis is perpendicular to the x, y plane, which includes the vector along the optical axis direction of the schlieren system. Also, n and n_b in Fig. 5 indicate the refractive index in the jet cross-section and that of the surrounding

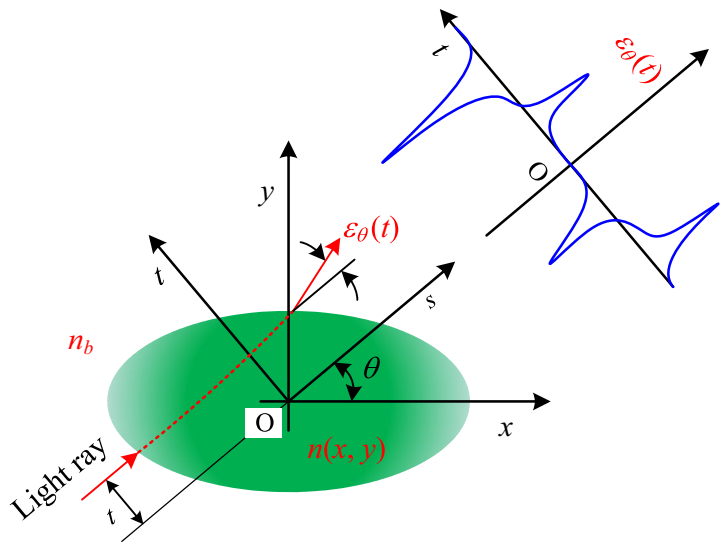

Fig. 5 A light ray passing through a certain cross-section perpendicular to the flow direction

air, respectively. Density fields are investigated for a cross-section at different axial locations.

As shown in Fig. 5, the rotated coordinates (s, t) are introduced at an angle θ away from the fixed-original coordinates (x, y). Then, a light ray traveling in the s direction with an offset of t from the axis s is bent by the interaction with the jet flow and has an angle of inclination $\varepsilon_\theta(t)$ with respect to its original path. The deflection angle $\varepsilon_\theta(t)$ after passing through the refractive index field of the incoming ray initially parallel to the s-axis is given by the Radon integral for small ray deflections as follows:

$$\varepsilon_\theta(t) = \int_{-\infty}^{\infty}\int_{-\infty}^{\infty} \frac{\partial \eta(x,y)}{\partial t}\delta(x\sin\theta - y\cos\theta + t)dxdy \tag{1}$$

where δ denotes the Dirac delta function, and $\eta(x, y)$ is the normalized refractive index difference given by

$$\eta(x,y) \equiv \frac{n - n_\mathrm{b}}{n_\mathrm{b}} \tag{2}$$

The $\varepsilon_\theta(t)$ is taken for a range of various angles from $\theta = 0$ deg to 180 deg.

The task of tomographic reconstruction in the present investigation is to find $\eta(x, y)$ based upon a given knowledge of $\varepsilon_\theta(t)$, and then, the density fields can be obtained through a well-known linear relation between the refractive index and the value of density, as described later.

The transfer from the (x, y) to (s, t) coordinate systems for the integral of the right-hand side of (1) leads to

$$\varepsilon_\theta(t) = \frac{\partial}{\partial t}\int_{-\infty}^{\infty} \eta(s\cos\theta - t\sin\theta, s\sin\theta + t\cos\theta)ds \tag{3}$$

After the one-dimensional Fourier transform of (3) with respect to the t variable and using the Leibniz rule for differentiation under the integral sign, it reduces to a relation,

$$\begin{aligned}
&\int_{-\infty}^{\infty} \varepsilon_\theta(t)\exp(-i2\pi t\zeta)\mathrm{d}t \\
&= 2\pi i\zeta \int_{-\infty}^{\infty}\int_{-\infty}^{\infty} \eta(s\cos\theta - t\sin\theta, s\sin\theta \\
&\quad + t\cos\theta)\exp(-i2\pi t\zeta)\mathrm{d}s\mathrm{d}t \\
&= 2\pi i\zeta \int_{-\infty}^{\infty}\int_{-\infty}^{\infty} \eta(x,y)\exp[-i2\pi(ux + vy)]\mathrm{d}x\mathrm{d}y
\end{aligned} \tag{4}$$

where i is the imaginary unit, ζ is the transform variable, $u = -\zeta\sin\theta$, and $v = \zeta\cos\theta$.

This equation expresses the two-dimensional Fourier transform of $\eta(x, y)$. Hence, the two-dimensional inverse Fourier transform of (4) and after some tedious calculations, it leads to

$$\begin{aligned}
\eta(x,y) &= \int_0^{\pi}\mathrm{d}\theta \int_{-\infty}^{\infty}\left(\int_{-\infty}^{\infty}\varepsilon_\theta(t)\exp(-i2\pi t\zeta)\mathrm{d}t\right) \\
&\quad \frac{|\zeta|}{2\pi i\zeta}\exp(2\pi i t\zeta)\mathrm{d}\zeta \\
&= \int_0^{\pi}\left[\varepsilon_\theta(t) * k(t)\right]_{t=-x\sin\theta+y\cos\theta}\mathrm{d}\theta
\end{aligned} \tag{5}$$

where $k(t)$ is a filter function with the Nyquist frequency, f_max, given by

$$k(t) \equiv \int_{-f_\mathrm{max}}^{f_\mathrm{max}} \frac{|\zeta|}{2\pi i\zeta}\exp(i2\pi\zeta t)\mathrm{d}\zeta = \frac{\sin^2\left(\pi t f_\mathrm{max}\right)}{\pi^2 t} \tag{6}$$

and the asterisk * denotes the convolution between $\varepsilon_\theta(t)$ and $k(t)$ (Agrawal et al. 1998).

When deflection data are sampled at a spacing of Δt, only frequencies below the Nyquist frequency $f_\mathrm{max} = 1/(2\Delta t)$ are adequately sampled. The ray deflection angle $\varepsilon_\theta(t)$ is correlated with the focal length f_d of

a decollimating lens and the ray transverse displacement $d_\theta(t)$ at the cutoff plane of the schlieren system as follows:

$$\varepsilon_\theta(t) = \frac{d_\theta(t)}{f_\mathrm{d}} \tag{7}$$

Equation (5) can be replaced by its discrete counterpart as

$$\eta(x,y) = \sum_{i=0}^{I-1} \frac{\pi}{I-1} \sum_{j=-J/2}^{J/2-1} \varepsilon_\theta(j\Delta t) \times k(y\cos\theta - x\sin\theta - j\Delta t)\Delta t \tag{8}$$

with $\theta = i\pi/(I-1)$ for I views of J rays each (Agrawal et al. 1998).

The refractive index $n(x, y)$ relates to the gas density $\rho(x, y)$ with the Gladstone–Dale constant K as

$$n(x,y) = 1 + K\rho(x,y) \tag{9}$$

Therefore, combination of (8) and (9) leads to

$$\rho(x,y) = \rho_\mathrm{b} + \frac{n_\mathrm{b}\eta(x,y)}{K} \tag{10}$$

The two-dimensional density field on the cross-section perpendicular to the central axis of the jet at a given position z in the streamwise direction can be obtained by (6) ~ (8), and (10). The same can be calculated sequentially in the downstream direction from the nozzle exit to form the three-dimensional density field $\rho(x, y, z)$ of the jet plume. Before reconstructing the density field using the CBP method, total variation (TV) filtering is applied for noise removal. The present rainbow schlieren system has a nominal spatial resolution of approximately 13 μm in the object plane, which can be evaluated based on the physical and image dimensions of the test nozzle (Kolhe and Agrawal 2009).

3 Results and discussion

3.1 Flow visualization

Time-mean rainbow schlieren pictures of a shock-containing elliptic jet operating at NPR = 4 are shown in Fig. 6 with the flow from left to right. The Reynolds number based on the equivalent diameter and flow properties at the nozzle exit is 3.0×10^5. These rainbow schlieren images were taken with the vertical filter setting, and hence, changes in the density gradient in the flow direction (z direction) can be observed.

Figure 6**a**, b shows the minor-axis and major-axis plane views of the elliptic jet. As shown at the top of the figure, the background hue H_0 corresponds to 237 deg, and in locations where the density gradient in the flow direction is large, H is smaller than H_0, and vice versa in locations where the density gradient is small. Note that rainbow schlieren images

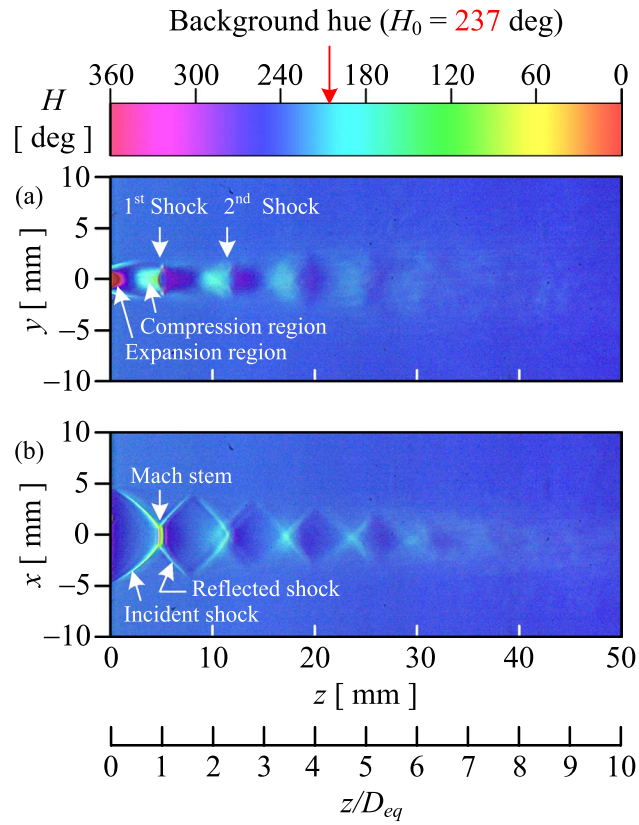

Fig. 6 Rainbow schlieren pictures with the vertical filter setting of the **a** minor-axis plane view and **b** major-axis plane view

taken in the absence of flow show the same hue across the entire field of view, which is the background hue. In addition, even in the presence of flow, the deflection angle of light passing through a location with zero density gradient is zero, so the hue value at that location is still the same as the background hue.

As indicated by the downward arrows in Fig. 6a, the consecutive shocks that are convex in the upstream direction can be observed at the locations where the first and second shock-cells almost terminate. As shown in Fig. 6b, the major-axis plane view indicates that the first shock is a Mach shock with a small Mach stem at the center of the jet. The Mach shock consists of upper and lower incident shocks generated immediately downstream of the nozzle exit lip and oblique shocks reflected at the endpoints of the Mach stem. It is not possible to determine from this schlieren image whether another Mach stem also occurs in the second shock-cell. The structure of the first shock and the subsequent downstream shocks are almost x-shaped and gradually decrease while maintaining a similar shape in the flow direction. The flow field downstream of the second shock-cell is indistinct. This would be attributed to a flapping mode oscillation about the major-axis plane (Edgington-Mitchell et al. 2015a, b, and Li et al. (2017)). To clearly observe the turbulent jet mixing

and shock oscillations sufficiently downstream of the nozzle exit, a high-speed camera with an even shorter exposure time than in this experiment should be utilized.

Time-mean rainbow schlieren pictures taken under the horizontal filter setting are shown in Fig. 7. The same color as the background hue can be observed radially far away from the jet centerline. This same hue is also seen at the jet centerline since the density gradient in the y-direction is zero (Al-Ammar et al. 1998). Notably, the rainbow filter used in the present experiment is not symmetrical with respect to the background hue. Thus, the hue distribution in Fig. 7 is not symmetrical around the jet center axis. In Fig. 7a, the shock shapes inside the jet are almost invisible, but the locations where the shocks interact with the jet shear layer can be observed. The free boundaries of the jets comprising the first and second shock-cells are clearly observed, but the jet boundaries further downstream are obscured by the y-directional oscillations of the jet. Figure 7b shows that the width between the upper and lower free boundaries of the jet gradually decreases in the flow direction. The grayscale schlieren picture taken by Edgington-Mitchell et al. (2015b) for an underexpanded jet issuing from an elliptic convergent nozzle of AR = 2 at approximately the same NPR as the present experiment, clearly shows strong slip lines from the Mach stem that persist for a significant distance downstream. However, no slip lines are visible in Fig. 7b. It is unclear at this time whether this is due to the influence of AR, the limitation of the measurement resolution, or the true characteristics of the flow.

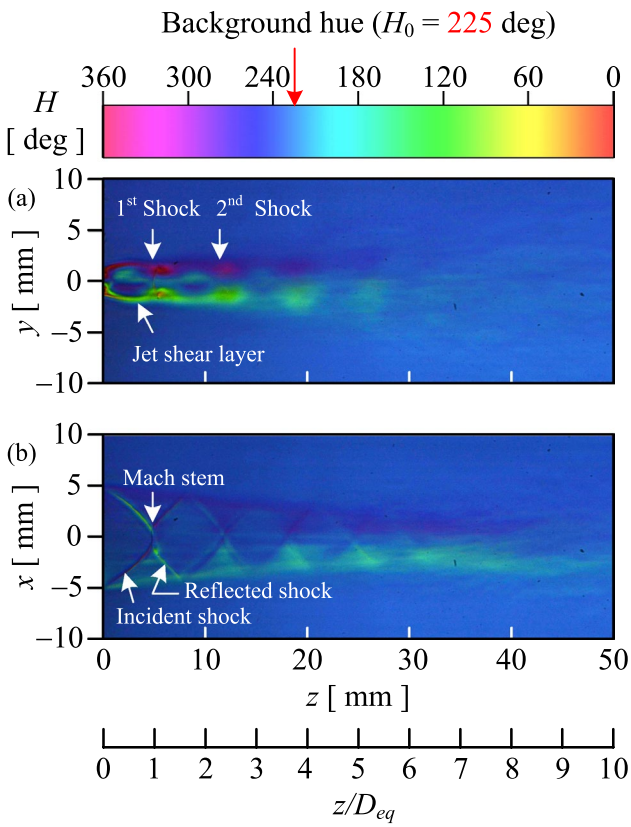

Fig. 7 Rainbow schlieren pictures with the horizontal filter setting of the **a** minor-axis plane view and **b** major-axis plane view

3.2 Density fields

The three-dimensional density field of the shock-containing elliptic jet is given in Fig. 8 with isopycnic representation, which shows surfaces of constant density inside the jet. Only iso-density surfaces where ρ/ρ_b = 1.2, 1.6, 1.9, and 2.4 are represented in blue, green, yellow, and red, respectively. The jet density field has a complex three-dimensional structure immediately after the nozzle exit, but becomes simpler downstream, showing a bowl-shaped structure symmetrical to the central axis of the jet sufficiently downstream.

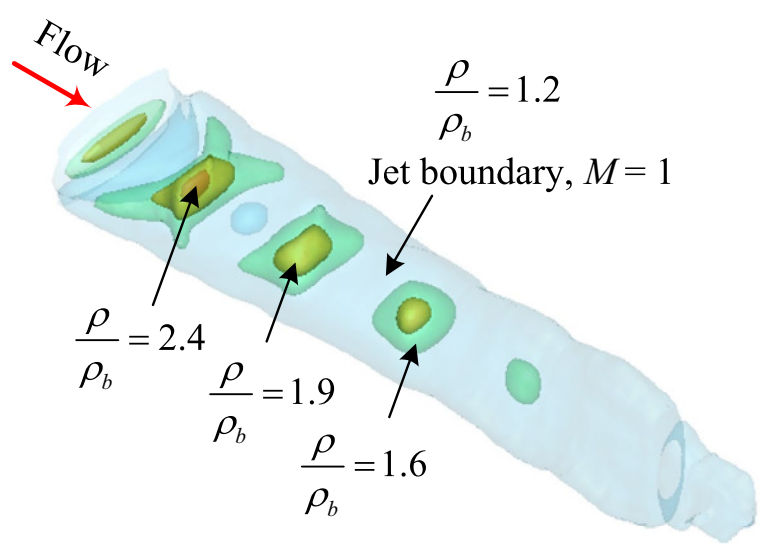

Fig. 8 Three-dimensional density field of a shock-containing elliptic jet: ρ/ρ_b = 1.2 in blue, 1.6 in green, 1.9 in yellow, and 2.4 in red. The flow Mach number M is unity at the jet sonic boundary showing ρ/ρ_b = 1.2

Menon and Skews (2010) defined the jet boundary shapes in nonaxisymmetric underexpanded jets as the outer surface on which the flow Mach number is unity within the jet because expansion or compression waves appearing in underexpanded jets are reflected at the free boundary of the jet where the Mach number is unity. We shall henceforth refer to this boundary as the jet sonic boundary. The shape of the jet sonic boundary can easily be obtained from the density field as follows:

Let p^* ($= p_b$) be the static pressure, T^* the static temperature, and ρ^* the density at the location where the flow Mach number is unity in the outer mixing layer of the jet. Since the entire flow field, including the inside of the nozzle, can be regarded as an adiabatic flow (André et al. 2014), the total temperature is constant everywhere, and hence, it equals to the atmospheric temperature T_b. Therefore, considering the gas equation of state, the normalized density ratio at the jet sonic boundary is given by

$$\frac{\rho^*}{\rho_b} = \frac{p^* T_b}{p_b T^*} = \frac{\gamma + 1}{2} = 1.2 \tag{11}$$

for $\gamma = 1.4$. This value is independent of NPR.

Only the second quadrant of Fig. 8 is shown in Fig. 9 to account for the symmetry of the jet, and the density contour plots in the minor-axis and major-axis planes are also included. The isopycnic surface displays the ranges from $x = -10$ mm to 0 mm, from $y = 0$ to 10 mm, and from $z = 0$ to 50 mm for the major-axis, minor-axis, and streamwise directions, respectively. The density field is normalized by the ambient density. The density range is indicated by the color bar at the top of the figure. The three-dimensional structure of the density field including the shock waves in the elliptic jet is clearly visible. As is evident from the schlieren images in Fig. 7a, b, Fig. 9 also shows that the jet sonic boundary gradually widens in the flow direction before reaching a peak value in the minor-axis plane, while it narrows in the major-axis plane.

The density contour plots in the minor-axis and major-axis planes of the elliptic underexpanded jet are illustrated in more detail in Fig. 10a, b, respectively. The flow direction is from left to right. Notably, these figures indicate the density fields on the cross-section including the jet central axis, but not those averaged along the viewing directions. The discontinuity lines above and below the jet plume at $z =$ approximately 36 mm in Fig. 10b are a kind of noise. The experimental data were processed with TV filtering before reconstructing the density field, but the noise could not be removed. Flow features such as curved shock in the minor-axis plane and incident shock in the major-axis plane are clearly observed in Fig. 10a, b. The width between the upper and lower jet sonic boundaries formed by the outermost density contour lines increases in the flow direction in the minor-axis plane, but decreases in the major-axis plane. A similar phenomenon was reported in experiments using Pitot tubes (Chauhan et al. 2015).

The streamwise variations in the widths (w_x and w_y) of the jet sonic boundary in the major-axis and minor-axis planes are shown in blue and red solid lines, respectively, in Fig. 11 where the curves are smoothed to remove fine noise. The w_x decreases linearly downstream from the nozzle exit and reaches zero at $z = 42$ mm. Moreover, w_y gradually increases in the downstream direction immediately after the nozzle exit and reaches a maximum at $z =$ approximately 31 mm as indicated by the solid circle, before decreasing to zero at $z = 42$ mm. A somewhat curious phenomenon, in which the jet

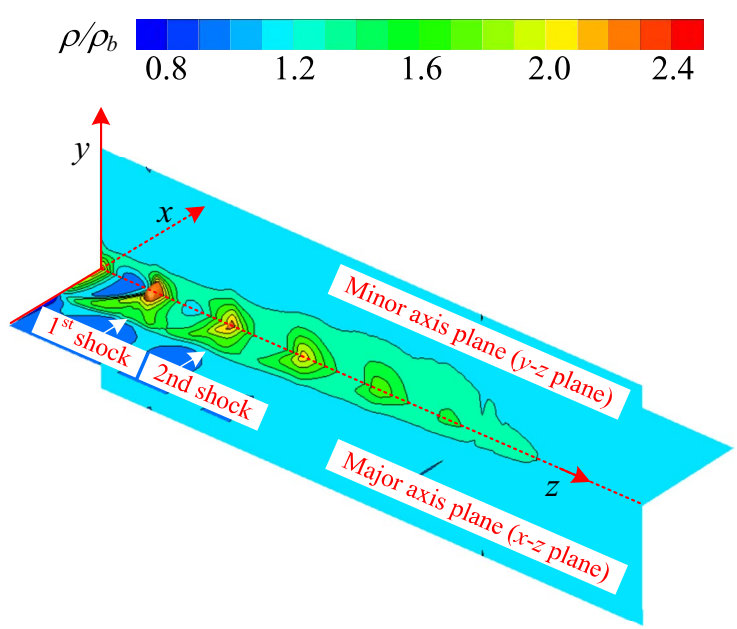

Fig. 9 Isopycnic surface with the contour plots in the minor-axis and major-axis planes

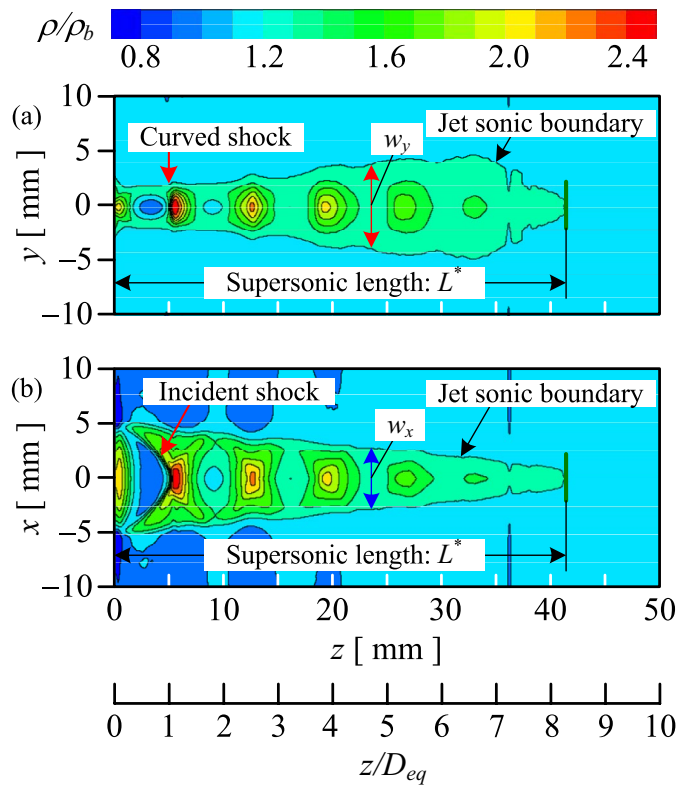

Fig. 10 Density contour plots in the **a** minor-axis plane and **b** major-axis plane

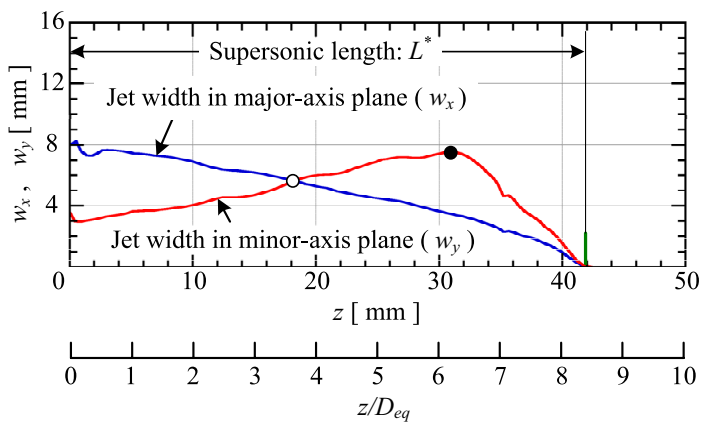

Fig. 11 Streamwise variations in the widths (w_x and w_y) of the jet sonic boundaries in the minor-axis and major-axis planes. The white and black circles denote the switchover and axis-switching locations, respectively

width (w_y) in the minor-axis plane suddenly decreases from z/D_{eq} = around 6, was also observed in Edgington-Mitchell et al. (2015), who reproduced the velocity field of an underexpanded jet issuing from an elliptic convergent nozzle of AR = 2 at NPR = 2.2 using PIV.

For incompressible elliptic jets, Hussain and Husain (1989) defined the jet half-widths in the minor-axis and major-axis planes as the transverse distance from the jet axis to the location where the mean velocity is half of the centerline value. It is difficult to quantitatively determine the axis-switching location from the jet half-widths. Instead, Hussain and Husain (1989) proposed a characteristic quantity called a switchover location, where the jet half-widths in the major and minor-axis planes become equal before the axis-switching occurs at a downstream location. For supersonic elliptic jets, Edgington-Mitchell et al. (2015) captured three-dimensional velocity field of an elliptic underexpanded jet by PIV. They examined the jet sonic boundary as well as the jet half-widths in the minor- and major-axis planes. Although not described in detail in their paper, it can be seen that the switchover location determined from the sonic boundary is approximately equal to that obtained from the jet half-widths. Aravindh Kumar and Rathakrishnan (2017) determined the switchover location (the original paper refers to it as axis-switching location) from the Pitot pressure profiles measured in the planes normal to the jet axis at different axis locations where the Pitot pressure is the

total pressure just behind the bow shock at the nose of the Pitot tube. However, they did not quantitatively define the jet boundary, leaving ambiguity in the determination of the switchover location. To the best of the author's knowledge, there are no studies that clearly define both switchover and axis-switching locations for elliptical nozzles. Therefore, in this study, the point where the jet sonic boundaries in the minor-axis and major-axis planes intersect with each other is defined as the switchover location, and the point where the jet sonic boundary in the minor-axis plane is at its maximum is defined as the axis-switching location. The switchover and axis-switching locations are indicated by open and solid circles, respectively, in Fig. 11.

The supersonic length L^* of underexpanded jets is defined as the distance on the jet central axis from the nozzle exit to the most downstream position where the flow Mach number is unity. This length can be determined as the streamwise distance from the nozzle exit to the position where the jet width is zero from the nozzle exit (Tashiro et al. 2023). Note that the potential core length, the supersonic core length, and the supersonic length are often used interchangeably, even though they are completely different concepts (Tashiro et al. 2023). In the current study, $L^* = 42$ mm or $L^*/D_{eq} = 8.4$ in the dimensionless form. The supersonic length obtained in this experiment would be useful in evaluating previous empirical relation. Perumal and Rathakrishnan (2021) proposed semi-empirical relations for the L^* in round and elliptic shock-containing jets, which include the equivalent diameter D_{eq} of the nozzle throat, the design Mach number M_d, the aspect ratio AR at the nozzle exit, the ratio p_e/p_b of the static pressure p_e to the back pressure p_b, and the specific heat ratio γ as governing parameters. For free jets issuing from elliptic convergent nozzles ($M_d = 1$), the normalized supersonic length L^*/D_{eq} can be expressed by

$$\frac{L^*}{D_{eq}} = \frac{e^{0.11\gamma M_j^2}}{\sqrt{\mathrm{AR}}}\left[-0.81\left(\frac{p_e}{p_b}\right)^2 + 5.43\left(\frac{p_e}{p_b}\right) + 0.03\right] \quad (12)$$

where M_j is the fully expanded jet Mach number, which depends on NPR as follows:

$$M_j = \sqrt{\frac{2}{\gamma - 1}\left(\mathrm{NPR}^{\frac{\gamma-1}{\gamma}} - 1\right)} \quad (13)$$

This relation was determined using experimental values obtained from Pitot probe and PIV measurements. When γ is constant, e.g., 1.4, Eq. (13) is a function of NPR and AR only, and it leads to

$$\frac{L^*}{D_{eq}} = \frac{e^{0.154M_j^2}}{\sqrt{\mathrm{AR}}}\left(-0.226\mathrm{NPR}^2 + 2.87\mathrm{NPR} + 0.03\right) \quad (14)$$

For NPR = 4, the nondimensional supersonic length derived from Eq. (14) with (13) is $L^*/D_{eq} = 5.7$, and it is approximately 32 % shorter than 8.4 for the present experiment. It is not possible at this stage to determine whether this discrepancy is due to differences in measurement techniques or to the fact that the semi-empirical relation is still inadequate. Note that in the original paper by Perumal and Rathakrishnan (2021), the supersonic length in the present paper is called the supersonic core length.

To determine the supersonic length from density fields, it is valuable to know the rough magnitude of density variations in the region near the jet sonic boundary. The ratio of density increment ($\Delta\rho$) to local density (ρ) can be expanded using the binomial theorem as a convergent power series (Shapiro 1953),

$$\frac{\Delta\rho}{\rho} = \frac{1}{2}M^2 + \frac{2-\gamma}{8}M^4 + \cdots \quad (15)$$

provided $(\gamma - 1)M^2/2$ is less than unity where the $\Delta\rho$ denotes the density difference between the local stagnation density and the local density. Therefore, the density increment ($\Delta\rho^*$) at the jet sonic boundary ($M = 1$), normalized to the ambient density (ρ_b), is given by

$$\frac{\Delta\rho^*}{\rho_b} = \frac{\rho^*}{\rho_b}\frac{\Delta\rho^*}{\rho^*} = 1.2 \times \frac{23}{40} = 69\% \quad (16)$$

for $\gamma = 1.4$. In addition, since the minimum Mach number (M_c) at which compressibility effects appear is $M_c = 0.3$ (Oosthuizen and Carscallen 1997), the corresponding normalized density variation ($\Delta\rho_c/\rho_b$) becomes

$$\frac{\Delta\rho_c}{\rho_b} = \frac{\rho_c}{\rho_b}\frac{\Delta\rho_c}{\rho_c} = 3.825 \times 0.0456 = 17\% \quad (17)$$

where ρ_c denotes the density corresponding to M_c, and isentropic flow is assumed in determining the ρ_c/ρ_b.

The density variations obtained from Eqs. (16) and (17) are sufficiently large compared to the precision errors in the present experiment, as described in Sect. 3.3. This means that the supersonic length in the present experiment is measured with sufficient accuracy. A recent study (Tashiro et al. 2023) using rainbow schlieren deflectometry to measure supersonic lengths of underexpanded microjets issuing from a round convergent nozzle would confirm that our argument is reasonable.

3.3 Streamwise density profiles

Three streamwise density profiles inside the elliptic jet including the jet central axis, the lipline in the minor-axis plane, and the lipline in the major-axis plane are shown in Fig. 12. Each density profile is represented with error bars indicating the uncertainty range where the error bars are spaced appropriately in the flow direction to prevent the figure from appearing cluttered. The errors in Fig. 12

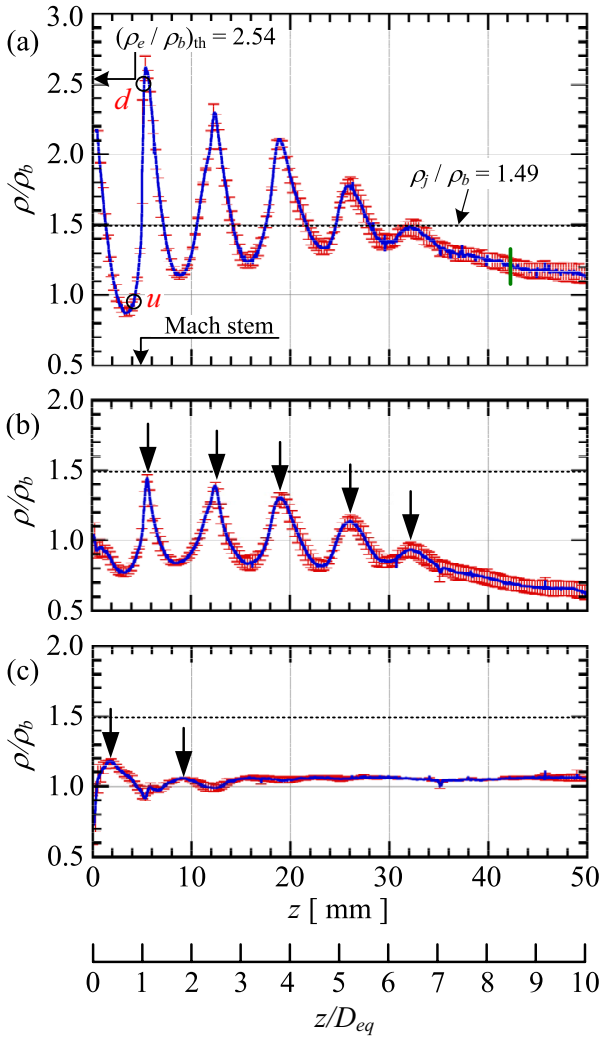

Fig. 12 Streamwise density profiles with uncertainty error bars along the **a** jet central axis, **b** lipline in the minor-axis plane, and **c** lipline in the major-axis plane

contain the precision error only, but not the bias error since it is negligibly small when compared to the precision error for density fields of shock-containing jets (Sugawara et al. 2020). To obtain precision errors, experiments were repeated five times. Subsequently, the standard deviation s of the sample of N measurements ($N = 5$ for the present experiments) was calculated by

$$s = \sqrt{\frac{\sum_{i=1}^{N} \left(\rho_i - \bar{\rho}\right)^2}{N-1}} \tag{18}$$

with $\bar{\rho} = \sum_{i=1}^{N} \rho_i / N$. The precision error s_p for the 95% confidence interval is defined as follows (Coleman and Steele 2009):

$$s_p = \frac{t_{95} s}{\sqrt{N}} \tag{19}$$

where t_{95} can be obtained from the student's t-distribution as $t_{95} = 2.78$ for $N = 5$. The average measurement uncertainties for the density profiles in Fig. 12a through Fig. 12c are within 2.6%, 2.2%, and 0.78% of ρ_b. The resolution of the rainbow filter used in the present study is about 9.4 µm, which corresponds to a minimum ray deflection angle of about 2.0×10^5 rad. Since the ray transverse displacement on the central axis of the jet is ideally zero, a minimum density value that can be captured by rainbow schlieren system is roughly related to the precision errors of the density on the jet centerline. For the present rainbow schlieren system, the minimum density value probably corresponds to 2.6% of the ambient density.

The leftward arrow on the ordinate in Fig. 12a indicates a theoretical value of $(\rho_e/\rho_b)_{th} = 2.54$, which is estimated based upon the assumption of the isentropic flow from the plenum chamber to the nozzle exit. The dashed line parallel to the abscissa in Fig. 12 denotes the fully expanded jet density $\rho_j/\rho_b = 1.49$ normalized by the ambient density (Sugawara et al. 2020). In addition, the streamwise location of the Mach stem estimated from the schlieren image in Fig. 6b is shown as the downward arrow on the abscissa. Furthermore, the short green line at $z = 42$ mm marks the location where the flow Mach number is unity. The streamwise distance from this location to the nozzle exit indicates the supersonic length (L^*).

As shown in Fig. 12a, the density along the jet central axis decreases rapidly in the flow direction from $z = 0$ due to the expansion waves generated at the nozzle exit lip, reaching a minimum value at a position just upstream of the Mach stem. Since the flow from the plenum chamber to just before the Mach stem is considered the isentropic flow, the freestream Mach number just before the Mach stem can be calculated as $M_u = 1.98$ at a location of the symbol "u" with the open circle, and the density just behind the Mach stem can be obtained as $\rho_d/\rho_b =$ approximately 2.50 from the normal shock relation (Rankin–Hugoniot's relation). This theoretical value is shown in Fig. 12a as the symbol "d" with the open circle. The theoretical value calculated by the normal shock relation is in good quantitative agreement with the present experimental value. This means that the RST demonstrates the ability to accurately capture strong shocks. The density downstream of the Mach stem repeatedly decreases and increases in the flow direction due to the successive shock-cells. However, since the shock strength is weaker downstream, the density amplitude is smaller in the flow direction. In the density profile along the central axis of the jet, the interval between the first and second peaks indicates the shock-cell length L_s (Tashiro et al. 2023). The L_s determined from Fig. 12a denotes 6.54 mm, and it is $L_s/D_{eq} =$

1.30 in the normalized form. The modified shock-cell model proposed by Nagata et al. (2022) leads to $L_s/D_{eq} = 1.26$, which almost matches the experimental value.

The densities on the lipline in the minor-axis plane are always below the dashed line from $z = 0$ to 50 mm. The five downward arrows denote the streamwise locations of the density maxima, which are approximately equal to the locations where the oblique shock waves inside the jet are reflected as expansion waves at the jet free boundary, as shown in Fig. 6a. On the other hand, only two density maxima at most can be observed in the density profile in the major-axis plane, as shown in Fig. 12c, because as seen from Fig. 6b, the shocks do not reach the locations of the lipline in the major-axis plane.

3.4 Shock structures and topology

The shock structures and topology in a shock-containing jet such as the spatial evolution of shock shape caused by shock-shock interaction or shock-expansion wave interaction can be revealed using the magnitude of the density gradient vector, given by

$$\frac{D_{eq}}{\rho_b}|\nabla\rho| = \frac{D_{eq}}{\rho_b}\sqrt{\left(\frac{\partial\rho}{\partial x}\right)^2 + \left(\frac{\partial\rho}{\partial y}\right)^2 + \left(\frac{\partial\rho}{\partial z}\right)^2} \tag{20}$$

in the non-dimensional form.

This representation can highlight areas with pronounced density gradients, such as shock waves, expansion wave origins, and jet shear layers (Sugawara et al. 2020). Figure 13b indicates a three-dimensional view of the shock structure generated inside the first shock-cell of the elliptical jet. Figure 13a, d demonstrates the shock structure viewed from the minor-axis and major-axis planes, respectively, and Fig. 13c, e denotes the front and rear views of the elliptic jet, respectively.

As shown in Fig. 13a, the incident shock generated near the nozzle exit lips has an isosceles triangle structure with a gradually widening width in the flow direction in the minor-axis plane. In the major-axis plane (Fig. 13d), the incident shock forms a crescent shape with a Mach stem near the center axis of the jet. Immediately after the incident shock and Mach stem, a short, reflected shock can be clearly seen. The incident shock becomes stronger as it gets closer to the

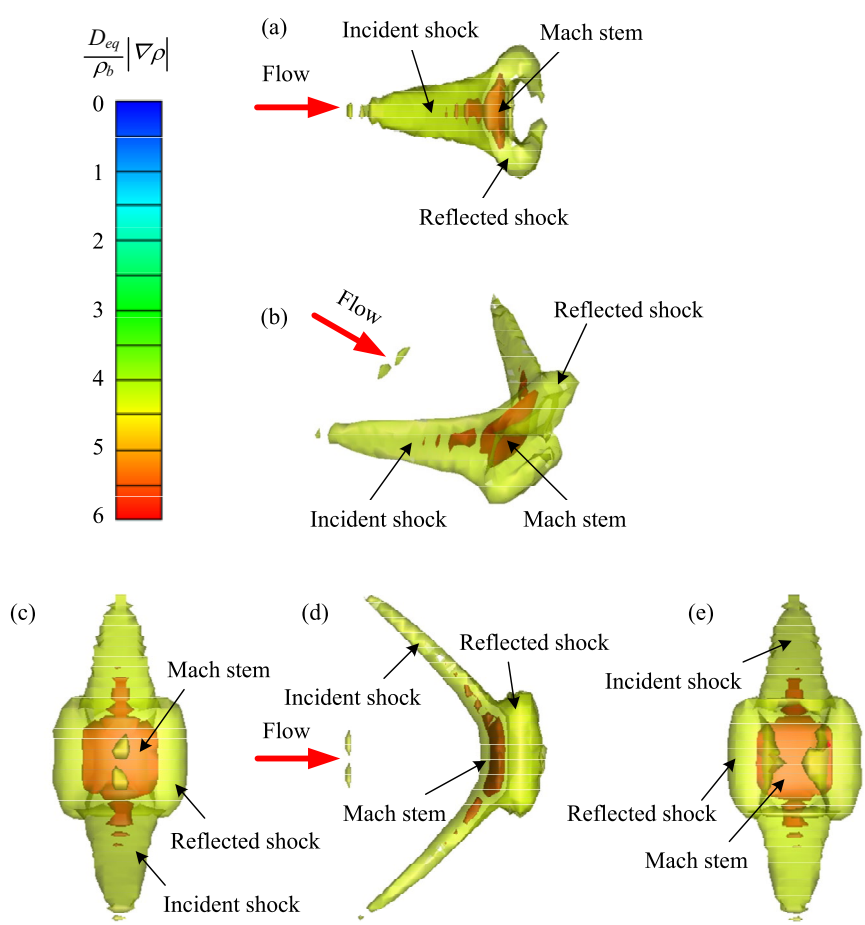

Fig. 13 Spatial evolution of the shock structures inside the first shock-cell with the **a** side view, **b** elevated view, **c** front view and **d** top view, and **e** rear view

Mach stem. Figure 13c, e shows that the Mach stem is a nearly square shape.

Three-dimensional structures of shock systems in an elliptical jet similar to those shown in Fig. 13b can be observed in the RANS simulations of Menon and Skews (2010) for AR = 2 and 4 under conditions at NPRs of approximately 3.8 and 5.7, and in the large eddy simulations of Li et al. (2017) for AR = 2 at NPRs of approximately 3.8 and 5.7. Notably, Menon and Skews (2010) and Li et al. (2017) did not validate their numerical code with quantitative experimental values on elliptical jets such as the density fields provided in this study. This is mainly due to the lack of available experimental data at that time. To the best of the authors' knowledge, Menon and Skews (2010) numerically demonstrated for the first time the shock structures and topology including the spatial evolution of the incident shock, reflected shock, and Mach stem.

4 Concluding remarks

Quantitative flow visualizations of an underexpanded jet emerging from an elliptic convergent nozzle with an aspect ratio (AR) of 4 and an equivalent diameter (D_{eq}) of 5.0 mm at the nozzle exit face were carried out using rainbow schlieren tomography (RST) for the first time. The experiments were performed at a nozzle pressure ratio (NPR) of 4 to produce strong shocks in the first shock-cell of the elliptic jet. Rainbow schlieren pictures of the elliptic jet were taken with the vertical and horizontal filter settings where a rainbow filter with finely variable hues within a width of 2.4 mm was used. The three-dimensional density field of the elliptic jet was reconstructed using the convolution back projection (CBP) algorithm with a nominal spatial resolution of approximately 13 μm.

The isopycnic surface of the shock-containing elliptic jet with density contour plots in the minor-axis and major-axis planes was provided to view the three-dimensional density field. The streamwise density profiles along the jet centerline as well as the liplines in the minor-axis and major-axis planes were also demonstrated. It was shown that the experimental density ratio across a Mach stem in the first shock-cell is in good quantitative agreement with the theoretical value estimated based on the normal shock relation, indicating that the RST quantitatively and accurately captures strong shock waves such as Mach stems. However, the slip line that would have resulted from the triple point of the Mach stem was not visible in the rainbow schlieren images with vertical and horizontal filter settings.

In the density field normalized by atmospheric density, the flow Mach number in the outer mixing layer of the jet becomes unity at the point where ρ/ρ_b is equal to 1.2 regardless of the NPR, indicating that the jet sonic boundary can be easily determined quantitatively. We proposed a method to quantitatively determine the switchover and axis-switching locations from the density field as follows: the point where the jet sonic boundaries in the minor-axis and major-axis planes intersect with each other indicates the switchover location, and the point where the jet sonic boundary in the minor-axis plane is at its maximum denotes the axis-switching location. In the present study, the switchover and axis-switching are located 3.6 and 6.2 times D_{eq}, respectively, downstream of the nozzle exit.

The previous semi-empirical relation for supersonic length (L^*) and the analytical solution for shock-cell length (L_s) were quantitatively evaluated by the present experimental data. As a result, the predicted supersonic length is 32% shorter than the present experimental value, and the analytical shock-cell length agrees well with the experimental value to within about 3%. The shock structures and topology of the near-field shock system were quantitatively demonstrated with the magnitude of the density gradient vector, showing that an incident shock is observed in the major-axis plane, but is absent in the minor-axis plane. The incident shock wave generated near the nozzle lip heads toward the central axis of the jet with increasing strength and width, forming a square Mach stem and a short reflected shock.

There are no theoretical solutions for elliptical jets with a strong shock such as a Mach stem. Therefore, results from other measurement techniques that can be quantitatively compared with the present data are strongly desired. In the near future, we plan to experimentally examine the effects of other ARs and NPRs on the flow features of elliptic underexpanded jets.

Acknowledgements The authors are deeply grateful to Tenta Tashiro of the University of Kitakyushu for his help in adjusting the rainbow schlieren optical system. The authors would also like to thank Dr. Takeshi Miyaguni of the University of Kitakyushu for the fabrication of the test nozzle using the 3D printer.

Author contributions SN and YM contributed to the conceptualization; TN contributed to the data curation, formal analysis, and visualization; TN and TS contributed to the investigation; TN contributed to the software; SN contributed to the resources and project administration; SN and YM contributed to the supervision; TN and TS contributed to the validation; and TN and YM wrote the main manuscript text. All authors reviewed the manuscript.

Funding This work was supported in part by a Grant-in-Aid for Scientific Research(C) (Grant No. 20K04272).

Availability of data and materials The data that support the findings of this study are available from the corresponding author upon reasonable request.

Declarations

Conflict of interest The authors report no conflict of interest.

Ethical approval Not applicable.

References

Agrawal AK, Wanstall CT (2018) Rainbow schlieren deflectometry for scalar measurements in fluid flows. J. Flow Vis. Image Process. 25:329–357

Agrawal AK, Butuk NK, Gollahalli SR, Griffin D (1998) Three-dimensional rainbow schlieren tomography of a temperature field in gas flows. Appl. Opt. 37:479–485

Akamine M, Teramoto S, Okamoto K (2023) Formulation and demonstrations of three-dimensional background-oriented schlieren using a mirror for near-wall density measurements. Exp Fluids 64:134

Al-Ammar K, Agrawal AK, Gollahalli SR, Griffin D (1998) Application of rainbow schlieren deflectometry for concentration measurements in an axisymmetric helium jet. Exp Fluids 25:89–95

Alvi FS, Krothapalli A, Washington D, King CJ (1996) Aeroacoustic properties of a supersonic diamond-shaped jet. AIAA J 34:1562–1569

Amjad S, Karami S, Soria J, Atkinson C (2020) Assessment of three-dimensional density measurements from tomographic background-oriented schlieren (BOS). Meas Sci Technol 31:114002

André B, Castelain T, Bailly C (2014) Experimental exploration of underexpanded supersonic jets. Shock Waves 24:21–32

Aravindh Kumar SM, Rathakrishnan E (2016) Characteristics of a supersonic elliptic jet. Aeronaut J 120:495–519

Aravindh Kumar SM, Rathakrishnan E (2017) Nozzle aspect ratio effect on supersonic elliptic jet mixing. ASME J Fluids Eng 139:101103

Chauhan V, Aravindh Kumar SM, Rathakrishnan E (2015) Mixing characteristics of underexpanded elliptic sonic jets from orifice and nozzle. J Propuls Power 31:496–504

Coleman HW, Steele WG (2009) Experimentation, validation, and uncertainty analysis for engineers, 3rd edn. Wiley, New York

Donaldson CD, Gray KE (1966) Theoretical and experimental investigation of the compressible free mixing of two dissimilar gases. AIAA J 4:2017–2025

Edgington-Mitchell D, Honnery DR, Soria J (2015) Multimodal instability in the weakly underexpanded elliptic jet. AIAA J 53:2739–2749

Edgington-Mitchell D, Honnery DR, Soria J (2015) Staging behavior in screeching elliptical jets. Int J Aeroacoust 14:1005–1024

Edgington-Mitchell D (2019) Aeroacoustic resonance and self-excitation in screeching and impinging supersonic jets—a review. Int J Aeroacoust 18:118–188

Feng T, McGuirk JJ (2016) Measurements in the annular shear layer of high subsonic and under-expanded round jets. Exp Fluids 57:1–25

Franquet E, Perrier V, Gibout S, Bruel P (2015) Free underexpanded jets in a quiescent medium: a review. Prog Aerosp Sci 77:25–53

Fukunaga R, Ezoe M, Nakao S, Miyazato Y (2022) Application of rainbow schlieren tomography for shock-containing rectangular jets. J Vis 25:687–695

Grauer SJ, Unterberger A, Rittler A, Daun K (2018) Instantaneous 3D flame imaging by background-oriented schlieren tomography. Combust Flame 196:284–299

Gutmark EJ, Grinstein FF (1999) Flow control with noncircular jets. Annu Rev Fluid Mech 31:239–272

Hussain F, Husain HS (1989) Elliptic jets. Part 1. Characteristics of unexcited and excited jets. J Fluid Mech 208:257–320

Islam MM, Nagata T, Nakao S, Miyazato Y (2024) Theoretical study of slightly underexpanded jets from elliptical nozzles. Trans Jpn Soc Aeronaut Space Sci 67:32–39

Kalyan A, Karabasov SA (2017) Broad band shock associated noise predictions in axisymmetric and asymmetric jets using an improved turbulence scale model. J Sound Vib 394:392–417

Kinzie K, McLaughlin DK (1999) Aeroacoustic properties of supersonic elliptic jets. J Fluid Mech 395:1–28

Kirby R (2018) Tomographic background-oriented schlieren for three-dimensional density field reconstruction in asymmetric shock-containing jets. AIAA Paper, 2018-0008

Kolhe PS, Agrawal AK (2009) Density measurements in a supersonic microjet using miniature rainbow schlieren deflectometry. AIAA J 47:830–838

Léon O, Donjat D, Olchewsky F, Desse JM, Nicolas F, Champagnat F (2022) Three-dimensional density field of a screeching under-expanded jet in helical mode using multi-view digital holographic interferometry. J Fluid Mech 947:A36

Nagata T, Islam MM, Miyaguni T, Nakao S, Miyazato Y (2022) Shock-cell spacings of underexpanded sonic jets emerging from elliptic nozzles. Exp Fluids 63:111

Nicolas F, Donjat D, Léon O, Le Besnerais G, Champagnat F, Micheli F (2017) 3D reconstruction of a compressible flow by synchronized multi-camera BOS. Exp Fluids 58:1–15

Li X, Zhou R, Yao W, Fan X (2017) Flow characteristic of highly underexpanded jets from various nozzle geometries. Appl Therm Eng 125:240–253

Maeda H, Fukuda H, Kubo K, Nakao S, Ono D, Miyazato Y (2018) Structure of underexpanded supersonic jets from axisymmetric Laval nozzles. J Flow Vis Image Process 25:33–46

Menon N, Skews BW (2010) Shock wave configurations and flow structures in non-axisymmetric underexpanded sonic jets. Shock Waves 20:175–190

Mitchell DM, Honnery DR, Soria J (2013) Near-field structure of underexpanded elliptic jets. Exp Fluids 54:1578

Mirjalily SAA (2021) Lambda shock behaviors of elliptic supersonic jets; a numerical analysis with modification of RANS turbulence model. Aerosp Sci Technol 112:106613

Oosthuizen PH, Carscallen WE (1997) Compressible fluid flow. McGraw-Hill, New York

Perumal AK, Rathakrishnan E (2021) Scaling law for supersonic core length in circular and elliptic free jets. Phys Fluids 33:051707

Rao AN, Kushari A, Mandal AC (2020) Screech characteristics of under-expanded high aspect ratio elliptic jet. Phys Fluids 32:076106

Sebastian R, Schreyer AM (2022) Flow fields around spanwise-inclined elliptical jets in supersonic crossflow. Eur J Mech B Fluids 94:299–313

Settles GS, Hargather MJ (2017) A review of recent developments in schlieren and shadowgraph techniques. Meas Sci Technol 28:042001

Shapiro AH (1953) The dynamics and thermodynamics of compressible fluid flow, vol 1. Wiley, New York

Streeter VL, Wylie EB, Bedford KW (2007) Fluid mechanics, 9th edn. McGraw-Hill, New York

Sugawara S, Nakao S, Miyazato Y, Ishino Y, Miki K (2020) Three dimensional reconstruction of a microjet with a Mach disk by Mach–Zehnder interferometers. J Fluid Mech 893:A25

Sugawara S, Nakao S, Miyazato Y, Ishino Y, Miki K (2021) Quantitative flow visualization of slightly underexpanded microjets by Mach-Zehnder interferometers. Flow Turbul Combust 106:971–992

Takano H, Kamikihara D, Ono D, Nakao S, Yamamoto H, Miyazato Y (2016) Three-dimensional rainbow schlieren measurements in underexpanded sonic jets from axisymmetric convergent nozzles. J Therm Sci 25:78–83

Tashiro T, Fukunaga R, Utsunomiya D, Nakao S, Miyazato Y (2023) Flow features of underexpanded microjets emerging from a round convergent nozzle. Exp Fluids 64:55

Urzay J (2018) Supersonic combustion in air-breathing propulsion systems for hypersonic flight. Annu Rev Fluid Mech 50:593–627

Yüceil KB (2017) A comparison of PIV and interferometric Rayleigh scattering measurements in the near field of underexpanded sonic jets. Aerosp Sci Technol 67:31–40

Zaman KBMQ (1996) Axis switching and spreading of an asymmetric jet: the role of coherent structure dynamics. J Fluid Mech 316:1–27

Publisher's Note Springer Nature remains neutral with regard to jurisdictional claims in published maps and institutional affiliations.

Springer Nature or its licensor (e.g. a society or other partner) holds exclusive rights to this article under a publishing agreement with the author(s) or other rightsholder(s); author self-archiving of the accepted manuscript version of this article is solely governed by the terms of such publishing agreement and applicable law.